Journal of
Marine Science and Engineering

MDPI

Article

Numerical Analysis of the Rudder–Propeller Interaction

Diego Villa *, Andrea Franceschi and Michele Viviani

Department of Electrical, Electronic and Telecommunications Engineering and Naval Architecture (DITEN), University of Genova, 16126 Genova, Italy; andrea.franceschi@edu.unige.it (A.F.); michele.viviani@unige.it (M.V.)

* Correspondence: diego.villa@unige.it; Tel.: +39-010-335-2345

Received: 10 November 2020; Accepted: 3 December 2020; Published: 4 December 2020

Abstract: The proper evaluation of the Rudder–Propeller interactions is mandatory to correctly predict the manoeuvring capability of a modern ship, in particular considering the commonly adopted ship layout (rudder often works in the propeller slipstream). Modern Computational Fluid Dynamics (CFD) solvers can provide, not only the performance of the whole system but also an insight into the flow problem. In the present paper, an open-source viscous flow solver has been validated against available literature experimental measurements in different conditions. After an extensive analysis of the numerical influence of the mesh arrangement and the turbulent quantities on the rudder provided forces, the study focused its attention on the forces generated by the rudder varying the propeller loading conditions and the mutual position between the two devices. These analyses give a hint to describe and improve a commonly-used semi-empirical method based on the actuator disk theory. These analyses also demonstrate the ability of these numerical approaches to correctly predict the interaction behaviour in pre-stall conditions with quite reasonable computational requests (proper also for a design stage), giving additional information on the sectional forces distribution along the span-wise rudder direction, useful to further develop a new semi-empirical rudder model.

Keywords: Reynolds Average Navier–Stokes (RANS); rudder–propeller interactions; validations and verification; actuator disk theory; rudder sectional forces

1. Introduction

The rudder is the most common steering device adopted to control the ship track. It is a lifting surface positioned, normally, in the stern ship region which, generating a lateral force, guarantees to perturb the ship direction. The correct design of its performance is mandatory to be able to control the ship's route and to obtain good manoeuvring and course-keeping ability of the ship, in particular, when auto-pilot or dynamic positioning capability are of interest ([1] or [2]). For safety reasons, at the beginning of the century, the International Maritime Organization (IMO) ([3,4]) required to satisfy mandatory manoeuvrability criteria for new ship constructions.

From a hydrodynamic point of view, it is a fairly simple device. It is a finite wing completely submerged (for big ships) with simple shapes. Despite its simplicity, in modern ships, in most cases it works in the propeller slipstream. This poses several issues in terms of predictability of hydrodynamic performance because its developed forces are not only correlated with the rudder characteristics (such as rudder span or chord size) but also with the propeller size and its working conditions (see [5]). Often, due to the complexity of the problem (further increased by the presence of the ship wake), traditional approaches based on semi-empirical mathematical models are still fashionable in the preliminary design stage, mainly due to their low computational demands ([6]). These approaches nowadays start to be overcome by fully viscous CFD codes which, however, are characterised by very high computational costs (see for instance [7]). In light of this, the traditional manoeuvrability

methods based on semi-empirical mathematical models ([8–10]) require not only a correct hull forces description ([11,12]) but also a complete and accurate model of rudder performance, able to provide their forces starting from kinematic quantities and known propeller settings.

In the past, several researchers worked on this topic using both experimental (among the others [13–16]) and numerical approaches. Different numerical approaches have been adopted in the reference literature, ranging from simpler potential ones (see for instance [17–21]) up to more demanding ones based on the complete flow equations ([7,22–24]). Particular attention should be paid also to hybrid methods, which try to merge the benefits of both approaches, consequently reducing the overall computational costs (among the others [5,25,26]).

The researchers who adopted numerical codes have focused their attention on different flow problems, ranging from the isolated rudder condition, often with peculiar rudder shapes ([14,15]) or when it interacts with a propeller ([27,28]). Others, on the contrary, considered the more complex problem which includes the mutual interactions of the complete system, i.e., rudder–propeller–hull (as in [24]).

This paper starts with a general overview of the numerical approach here adopted in Section 2, followed by a description of the reference rudder and the test conditions considered (Section 3). Then, after the description of the used propeller model and an in-depth comparison with the actuator disk theory in Section 4, the open-water rudder performances are compared with available experimental measurements (Section 5) focusing attention on the influence on the simulation results caused by the mesh arrangement and the turbulent quantities. These preliminary results provide the basic model set-up for the successive numerical and experimental comparisons when the rudder operates behind the propeller in different reciprocal positions (Section 6). These results provide the key to analyse and update a widely-used mathematical model for predicting the rudder forces behind a propeller (Section 7). Section 8 shows further analyses extracted by the CFD results analysing the rudder sectional forces, these can be used to better describe how the rudder–propeller interactions occur. Finally, some conclusions are presented in the last section.

2. Numerical Background

Several viscous codes are nowadays available to assess the performance of a moving finite wing immersed in a fluid. In the present paper, the open-source CFD library OpenFOAM has been considered as flow solver. This code has been demonstrated to be able to tackle marine problems with high quality results (see for instance [29–31]). It is designed to solve the flow field characteristics by adopting a general polyhedral mesh with a finite volume approach. The classical Navier–Stokes equations, which are here presented in time-varying form for an incompressible flow (see Equation (1)), are used taking advantage of the classical Reynolds decomposition to account for the turbulent effects.

$$\begin{cases} \nabla \cdot U = 0 \\ \rho \dfrac{\partial U}{\partial t} + \rho(U \cdot \nabla U) = -\nabla p + \mu \nabla^2 U + \nabla T^{Re} + S \end{cases} \tag{1}$$

where ρ and μ are the average density and molecular viscosity of the fluid, respectively, which, for the present case, have been considered constant in time and space, therefore, under the incompressibility assumption. U and p are the main flow characteristics: respectively velocity and pressure fields. These quantities have been averaged following the Reynolds decomposition, which adds in the momentum equation a turbulent stress tensor (T^{Re}) properly defined to account for the turbulent effects on the mean flow fields. The present equation form further includes a momentum source term (S), which is devoted to adding external mass forces into the motion equations. The latter term, commonly considered to include gravitational forces, is one of the key features here adopted to consider the propeller effect in the viscous simulations, without completely discretising its geometry.

The propeller effect has been, therefore, simulated following the same procedure already proposed in [5,32]. Instead of including the real blade geometry, which consequently requires a very dense

mesh in that region and a proper solver able to consider the propeller revolution rate (as sliding or overlapping mesh approaches), a simple force field can be considered in place of the propeller disc. This approach mimics the well-known immersed-boundary method (IB first proposed by [33]) further avoiding to resolve also the blade forces. As demonstrated in previous works (see [5]), although the local force unsteadiness (mainly due to the blade vortices interacting with the rudder, see also [34,35]) is out of the aim of the study (as for this case), only a reliable mean force distribution is required to reproduce the mean flow field behind the propeller correctly. Regarding the numerical set-up for the rudder performance evaluations (see Figure 1), a box domain with the same cross-section of the experimental wind-tunnel facility (see next section) is used. The inlet and outlet surfaces have been positioned sufficiently far enough (2.2 m upstream and 3.8 m downstream the rudder position) to avoid unwanted influences, and a symmetry condition has been imposed for the far-field boundaries (red surfaces in Figure 1). A prescribed velocity and pressure field have been imposed at the inlet and outlet, respectively, and for all the other wall surfaces (rudder and lower surface, in yellow in the figure), a wall condition is imposed. A mesh of about 1.5 million cells has been obtained. Further details, together with the mesh dependence analysis are reported in a previous work [5], and not repeated here for the sake of brevity.

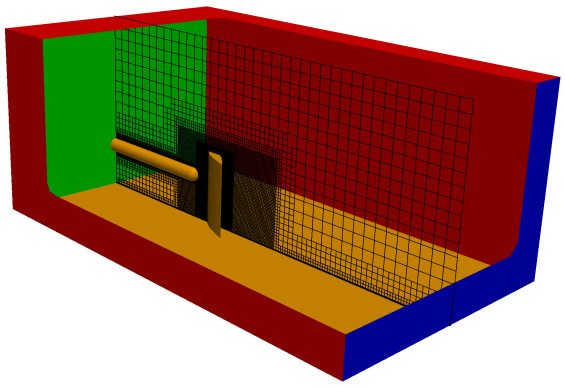

Figure 1. Sketch of the adopted mesh for the rudder with propeller simulation.

3. Test Cases

A considerable amount of experimental data is available in the literature dealing with the forces experienced by rudders. The most complete ones are the experimental measurements performed by [16,36]) at the Southampton low-speed wind tunnel over several years. They adopted a simple spade rudder characterized by a constant sectional profile defined by the NACA 4 digit series (NACA0020). The rudder dimensions were 1 m span and a constant chord of 0.667 m (see Table 1). Therefore, a rectangular rudder longitudinal profile was considered. Even if this shape is far from real rudder shapes nowadays used for ships, thanks to the extensive measurements performed by different authors, this series is an excellent numerical benchmark.

Table 1. Rudder main data (named N.2 in the original paper).

Data	Value	Unit
Section	NACA 0020	-
Span	1	m
Chord	0.667	m
Effective A.R.	3	-
t/c	0.2	-
Taper Ratio	1	-

The rudder was mounted in tandem with a propeller (as depicted in Figure 2). This particular experimental setup adopted allows to explore several rudder/propeller configurations (for instance varying their relative positions).

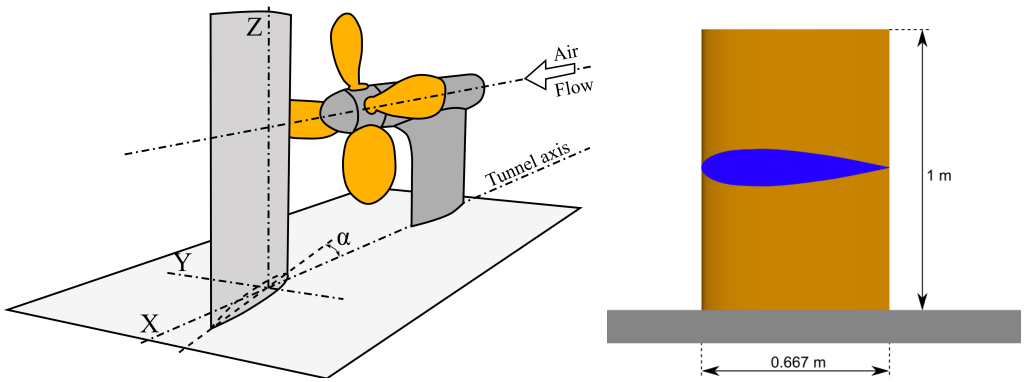

(**a**) Sketch of the Experimental setup (**b**) Plan view of the rudder (CFD model)

Figure 2. Rudder overview and main data.

The propeller was a modified Wageningen B4-40 propeller made of fibre-glass (see Table 2), more details can be found in reference literature [37]. The experimental measurements covered two flow speeds (10 and 20 m/s, equivalent to 4.4×10^5 and 8.8×10^5 Reynolds number respectively) and a wide range of angles of attack in a wind tunnel with a rectangular test section of about 3.5 × 2.5 m.

Table 2. Propeller main data (Modified Wageningen B4.40 Series).

Data	Value	Unit
N. blades	4	-
Diameter	0.80	m
Hub Diameter	0.20	m
P/D	0.95	-
Rake	0	-

4. Analysis of the Effectiveness of the Propeller Approach

When a rudder operates in the propeller slipstream (the usual arrangement for modern ships), its performances is strongly related to the propeller working point. For this reason, as a first step, it is mandatory to show the propeller model capability and accuracy here adopted. As mentioned previously, the time-averaged flow field generated by the propeller has been included in the viscous simulations via a body force approach. This approach guarantees to correctly reproduce the flow acceleration generated by the propeller (if the correct force distribution is considered) with a minimal increase of computational requests. This model, to correctly work, must be fed with the blade load distribution obtained by preliminary CFD open-water results. Different numerical methods (in some cases simplified and not very time consuming) can be used to generate the correct blade load, see for instance the ones based on the potential theory (lifting lines, lifting surfaces or Boundary Element Methods) or the ones based on the blade element momentum theory. All these approaches require a small additional computational effort (compared to a viscous solver), so they could also be applied for extensive analysis at all ship design stages. A fast and accurate viscous flow solver has been adopted here. Its numerical set-up can be found in previous works (see for instance [38,39]), not here reported for brevity. Through this type of solver, a quite wide range of advance coefficients ($J = \frac{V}{n \cdot D}$) can be easily computed with adequate confidence.

Figure 3 shows the comparison of the computed non-dimensional thrust, torque and load ($\frac{K_T}{J^2}$) coefficients with respect to all the measurements reported in [16] for the here adopted propeller.

All the EFD data come from different tests (different revolution rates and flow speeds), consequently, showing also the uncertainty range of the measurements. An overall good agreement between the predictions and the measurements can be highlighted from the figure, demonstrating the reliability of the proposed CFD simulations. Only the torque shows a slight underestimation, mainly due to the small Reynolds number adopted in the experiments. Anyway, for the sake of completeness, the torque values are not so correlated with the propeller/rudder interaction effects in term of lift as shown in last part of this work; therefore, these discrepancies can be neglected. In light of these considerations, the blade load distribution, defined as the sectional longitudinal and tangential forces provided by the blades, has been extracted from the simulations. Three characteristic working conditions, the design one (about $J = 0.5$) and two off design ones (about $J = 0.3$ and 0.9), have been considered. The obtained distributions are depicted in Figure 4, reporting both the longitudinal and tangential contribution with respect to the sectional forces generated by the blades.

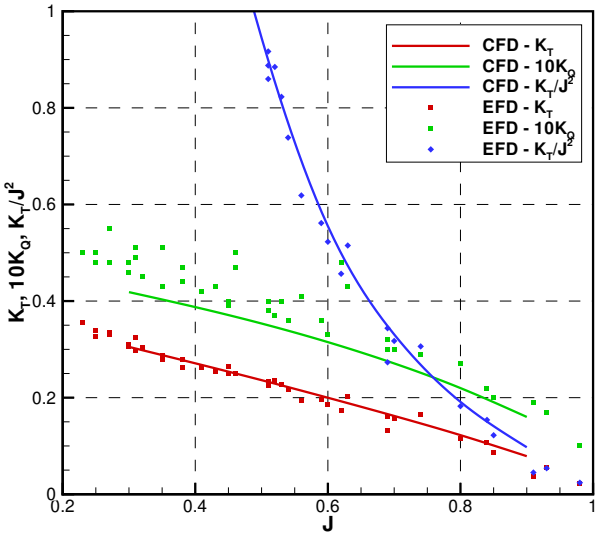

Figure 3. Numerical and experimental comparison of thrust and load coefficients.

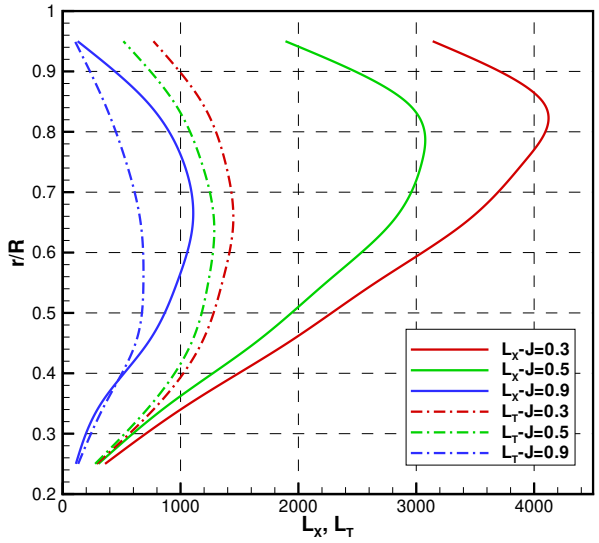

Figure 4. Longitudinal (solid) and tangential (dashed) sectional forces at three advance coefficients with high (J = 0.3), low (J = 0.9) and medium (J = 0.5) loads.

Figure 4 clearly shows that decreasing the advance coefficient, the load distribution increases, shifting its maximum upward (in the radial direction). Ref. [5] already showed this effect, where, for the same propeller, the bollard pull condition was considered. In that case, the maximum load value was positioned almost at the blade tip. Similar behaviour also involves the tangential component (the one which generates the torque experienced by the propeller), which, differently from the axial component, is often characterized by a peak positioned nearer to the hub (at about half the blade span).

In the literature, the overall propeller effect on the flow field is normally represented by the actuator disk theory. Based on this theory, the flow acceleration index a (defined as the ratio between the induced velocity in the propeller disk and the inflow speed) provided by a propeller is a function (see Equation (3)) of the thrust coefficient defined in (2).

$$C_T = \frac{T}{1/2\rho(\pi R^2)V^2} \tag{2}$$

$$a = \frac{1}{2}(\sqrt{1 + C_T} - 1) \tag{3}$$

where R stands for the propeller radius and T and V are respectively the propeller thrust and the average in-flow velocity to the propulsor. These increased velocities can be found inside the tube flow generated by the propeller disk. The shape of this tube, and the average velocities inside it, can be approximated by the following Equations (4) and (5) respectively.

$$D(x) = D\sqrt{\frac{1+a}{1+K_P \cdot 2a}} \tag{4}$$

$$U(x) = V(1 + K_P \cdot 2a) \tag{5}$$

where a is the acceleration index computed in Equation (3), D is the propeller diameter and V is the undisturbed speed. Their behaviours are therefore proportional to the K_P coefficient, dependent upon the non-dimensional distance (x) between the propeller and the rudder with respect to the propeller radius. The coefficient K_P ranges between 0 for $x \to -\infty$ and 1 for $x \to \infty$. Moreover, it assumes the value of 0.5 for $x = 0$. A possible approximation of the variation of K_P with the longitudinal position is:

$$K_P(x) = 0.5 + 0.36 \times \tanh(0.98x) + 0.11 \times \tanh(15x) \tag{6}$$

Other formulations exist for these quantities like the one proposed by Brix in [40], which generates (only for the propeller slip-stream region) a quite similar behaviour.

The experimental activities focus their attention on three propeller working conditions characterized by different propeller loads ($K_T/J^2 = 0.05, 0.88, 2.3$). In light of this, a simple simulation with only the propeller, represented via the body force approach, has been carried out imposing the corresponding thrust and torque. These simulations have been carried out considering the rudder domain, but excluding the rudder surface. Each simulation adopts the proper thrust and torque radial distribution previously mentioned. Figure 5 shows the computed velocities (made non-dimensional by means of the acceleration index a times the inflow speed) in the propeller disk for the three loads considered. These behaviours qualitatively well match the flow measurements reported in [41,42] that show, for different propeller shapes at high load conditions, the radial distributions of velocities in the propeller slipstream. Two considerations need to be exposed: first the obtained velocities in the propeller plane due to the body forces, well match with the actuator disk theory globally (the three curves match one each other); second, the different adopted load distributions slightly change the radial velocity distributions generated by the models. In fact, when higher load is considered, also the velocity behaviour shows its peak slightly shifted to the higher radii as expected. In the range between $r/R = \pm 0.25$, due to the presence of the hub, the data has been forced to zero value. In addition, an overall velocity reduction can be seen out of the propeller disk, mainly due to the 3-dimensional

effects of the body force approach. For the sake of completeness, it has to be kept in mind that this particular model can only reproduce the overall propeller effect, not its flow details (as tip or hub vortex or similar features), as for instance, the induced axial velocity due to the flow swirl.

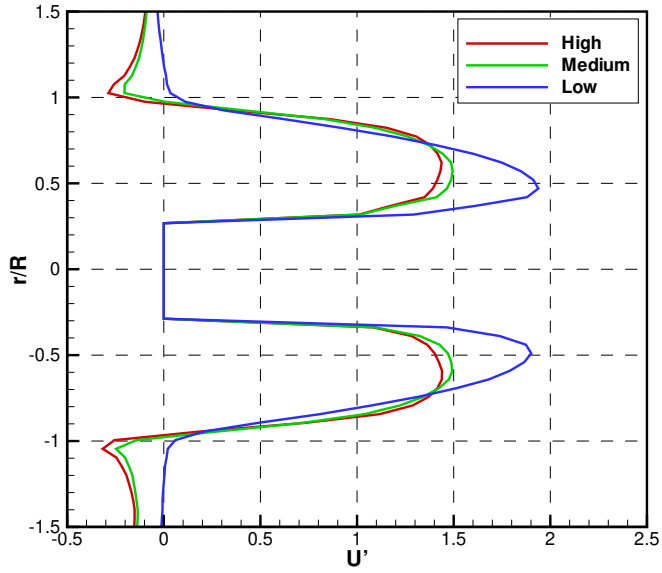

Figure 5. Non-dimensional induced velocity distributions in the propeller plane for the propeller body force simulations at three considered loads.

As mentioned previously, the two theoretical tube flow behaviours can be compared to the one extracted from the CFD simulations. The CFD values have been obtained evaluating the mass flow rate in correspondence of the propeller plane (where the diameter is known), then, imposing its conservation, for each section at a different longitudinal position, the diameter and the average speed can be easily obtained. Figure 6 reports this comparison for the three loads adopted, showing that all the approaches (mathematical models and CFD ones) well describe the typical wake contraction and consequently, due to the conservation of the mass flow rate, the mean velocities increasing accordingly. Moreover, this comparison shows two important aspects: first as expected, the computed flow behaviour is not exactly the same as the two proposed formulations: the CFD simulations predict faster diameter contraction than the ones proposed by Brix; second, in the down-stream region the diameter does not become constant but slightly increases. This latest effect can be ascribed partially to the presence of the hub wake, and partially to a diffusion effect (also connected with the turbulent mixing effect) whose importance increases proportionally with the velocity jump between inside and outside the tube. This latter effect, already mentioned by Brix in [40], is well visible in Figure 7, where the longitudinal computed velocities at different positions (from 0.75 to $2x/D$) are depicted together with the tube flow characteristics. Moving to the propeller slipstream, the velocity jump from the propeller accelerated flow field to the external undisturbed flow tends to diffuse, making the tube diameter slightly bigger than the theoretical one (reported as dashed and doted lines). For the sake of completeness, it has to be pointed out that the reported numerical results, with respect to the theoretical ones, are affected by a small blockage effect due to the ratio between the propeller area and the cross-section of the virtual tunnel. Following the well-known Glauert Correction [43], the flow speed variation is estimated less than 3% for the higher load considered; therefore, it can be considered negligible.

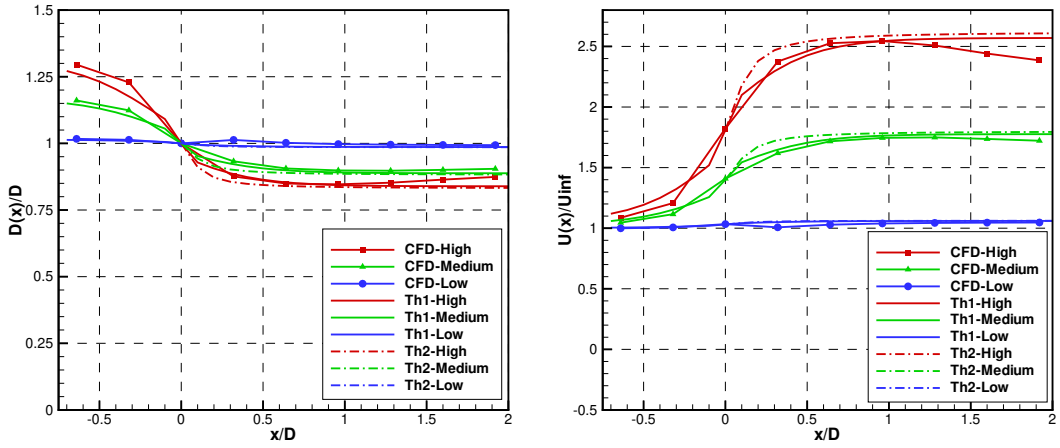

(**a**) Diameter (**b**) Average Velocity

Figure 6. Comparison of the CFD non-dimensional tube flow quantities versus the longitudinal distance for the three loads versus two theoretical formulations (solid line from reported equations and dashed lines from Brix formulation).

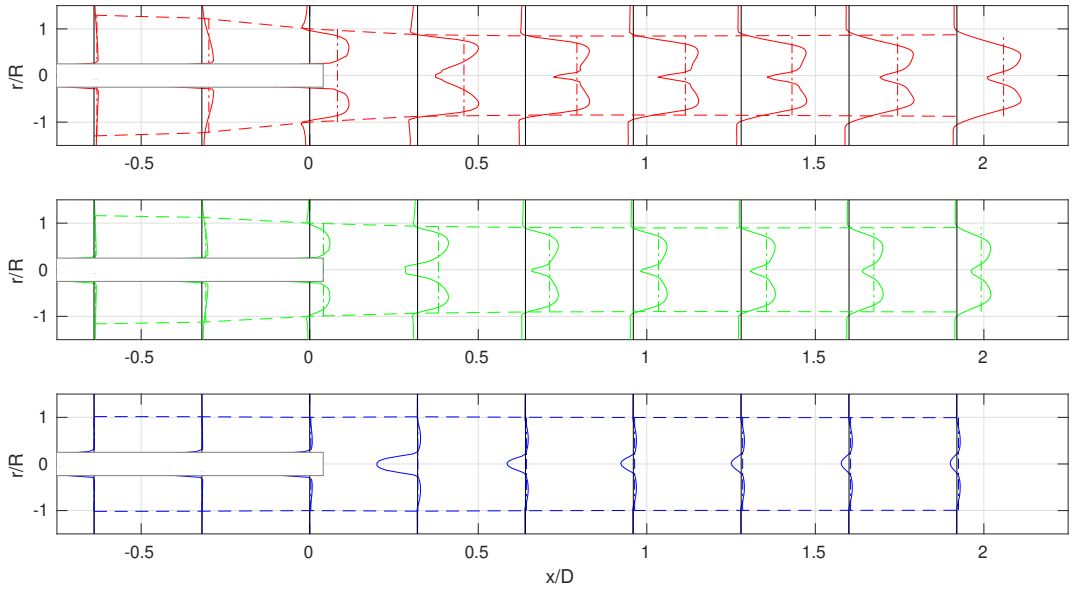

Figure 7. Non-dimensional longitudinal velocity distributions for the propeller body force simulations.

5. Open-Water Rudder Analysis

A preliminary validation of the CFD viscous code's ability to correctly predict the rudder open-water characteristics under different flow conditions has been already shown in [5]. Here, to enlarge that analysis, some additional simulation parameters have been investigated: the inflow turbulence and the near-wall treatment. The main drawback highlighted in previous research was related with the ability of the CFD simulations to correctly predict the stall inception occurrence. Even though several studies can be found on the rudder forces, most of them do not focus their attention on the stall inception angle. Considering that the stall phenomenon is due to a flow instability, which detaches the near wall stream line from the rudder back profile, it is difficult to be numerically predicted due to its intrinsic unstable nature. In addition, from an experimental point of view, some hysteresis effects, strongly connected to the inflow turbulence, can occur (see [44]), making the rudder force evaluation at higher radii subject to significant variations. Often, particular numerical approaches are used to consider this effect, but they are mainly based on complex experimental calibrations. To elaborate on this topic using numerical calculations, some systematic analyses have

been carried out on two numerical aspects: the influence of the inflow turbulence and the first-cell wall-layer treatment. The simulations adopted here are based on the well-known SST $k-\omega$ turbulence model. This model is widely adopted for external flows characterized by both attached and separated flow conditions. From a physical point of view, when an external flow is considered, it is mandatory to prescribe realistic inflow turbulence quantities. The reference literature shows that the turbulent quantities at the inlet influence most of the usually used turbulent models. Among all the possible choices, the Turbulent Intensity (I) and the Eddy Viscosity Ratio (E) are here considered. The first one represents the amount of mean velocities fluctuations with respect to the mean flow speed. Depending on the physical conditions considered, it can assume several values: ranging from 5% to 20% for flows in complex geometries and less than 1% if a very stable inflow field is considered (almost absent inflow turbulence). Regarding the here considered simulations, values between 1% and 10% can be expected: lower values inside the wind tunnel and higher ones behind a ship wake. The second parameter, the Eddy Viscosity Ratio, estimates the effects of the turbulent viscosity with respect to the molecular one. This value is hard to estimate, and generally, its value can range from one to one thousand. These quantities, therefore, can be used to estimate the inflow turbulent model parameters via the typical literature Equation (7) with respect to the means inflow speed U.

$$k = \frac{3}{2}(IU)^2 \quad \text{and} \quad \omega = \frac{k}{\nu E} \tag{7}$$

Considering that no experimental measurements have been reported in the reference literature, neither in the wind tunnel nor behind a ship, for these quantities, several simulations have been carried out to explore the sensitivity of the proposed numerical model to a quite wide range of these parameters. Two different types of simulations have been considered: the first one adopts a boundary layer mesh designed in order to take advantage of the wall-functions in the first near-wall cells, therefore its $Y+$ value (the non-dimensional distance of the first cell from the wall) is about 30; the second one, on the contrary, adopts a wall-resolved boundary layer, so with a $Y+$ value always lower than 1.

Figure 8 shows the two adopted meshes. The one which models the boundary layer has only 4 layers of cells characterized by a quite low aspect ratio; on the contrary, the wall-resolved one has 10 layers with a quite high grading (about 1.6). From a hydrodynamic point of view, both the meshes follow state-of-the-art for the solution of the boundary layer problem.

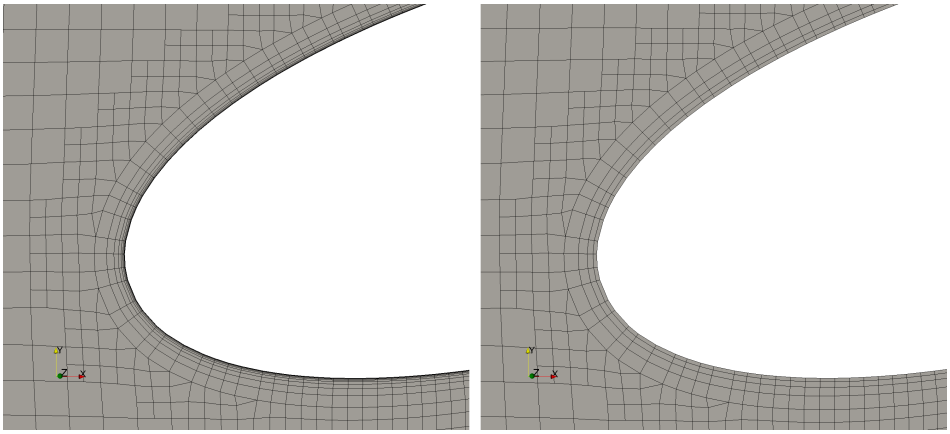

Figure 8. Details of the boundary layer mesh arrangement for the two types of simulations: wall-modelled (**Right**), wall-resolved (**Left**).

Figure 9 shows the simulation results for the two mesh arrangements compared with the experimental values. Regarding the EFD data, not only the simulated flow speed (10 m/s) is reported but also the higher one (20 m/s) for comparison. These two sets of data can give an overview of the expected experimental uncertainty also concerning the turbulent quantities. In the linear region,

the two measures show almost identical values, but when the stall occurs, the two data differ significantly. Analysing the obtained results, it is evident that the CFD predictions give the same results in the pre-stall region. Only when very high values of turbulence (I = 10% and E = 1000) are considered, a slightly over-prediction of the lift occurs. When the rudder stalls the two meshes work differently. The wall-modelled one abruptly anticipates the stall inception (of about 5 degrees) for all the turbulence parameters here adopted. Moreover, the turbulent parameters slightly affect the lift behaviour also after the stall, showing a maximum standard deviation among the series of 0.026. Differently, accurately predicting the boundary layer characteristics, a better agreement can be observed between the CFD and EFD results also in terms of stall inception. In fact, the predicted stall inception angle is shifted towards 20 degrees.

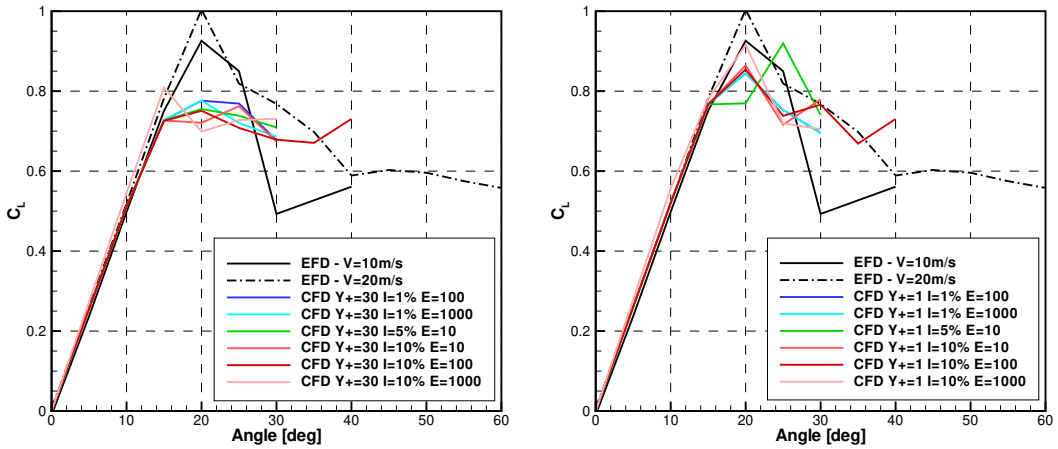

(**a**) Wall-modelled simulations ($Y+$ = 30) (**b**) Wall-resolved simulations ($Y+$ = 1)

Figure 9. Non-dimensional lift force predicted at 10 m/s vs. EFD measurements.

Considering the previously mentioned conclusion related to the high turbulence values, a systematic analysis of their effect on the stall inception has been performed on the wall resolved mesh arrangement. To better analyse the problem, the results have been refined every 2.5 degrees in the range between 15 to 25 degrees. Figure 10 collects the systematic results varying the turbulent viscosity ratio from 1% to 10% and the turbulent intensity from 1 to 10. These results show again that the proposed model well predicts the force behaviour in the pre-stall zone (from 0 to 15 degrees) but, when the stall occurs (15 to 25 degrees), a great force variability is found. Moreover, again, no clear correlation between the force behaviour and the turbulence parameters can be drawn from these figures. Among all the results, the simulation which best approximates the EFD measurements (compared with the value at the same flow speed of 10 m/s) is the one with turbulent values equal to $I = 2\%$ and $E = 10$. Therefore, these values have been selected for all the following analyses.

In conclusion, the wall-resolved model better predicts the stall inception but with a quite significant sensitivity on the turbulent parameters. In other words, if the pre-stall region is of interest, both the approaches (wall-resolved and wall-modelled) give the same accuracy with the only constraints to avoid too high turbulent values (maybe unfeasible) of the inflow. For the sake of completeness, two aspects should be considered: first, all the here reported simulations are steady, consequently, the post-stall region can not be accurately computed because the transient effects are neglected; second, in the previous activity ([5]), also the mesh density had been varied showing the inability of this numerical approach to capture the post-stall phenomena also with a finer mesh. Considering that the main aim of the present paper was to investigate the interactions between the propeller and the rudder for manoeuvring purposes, the here reported results can be considered adequate enough. The following reported simulations adopt the wall-resolved model, which proves to be able to capture the physics of the problem better.

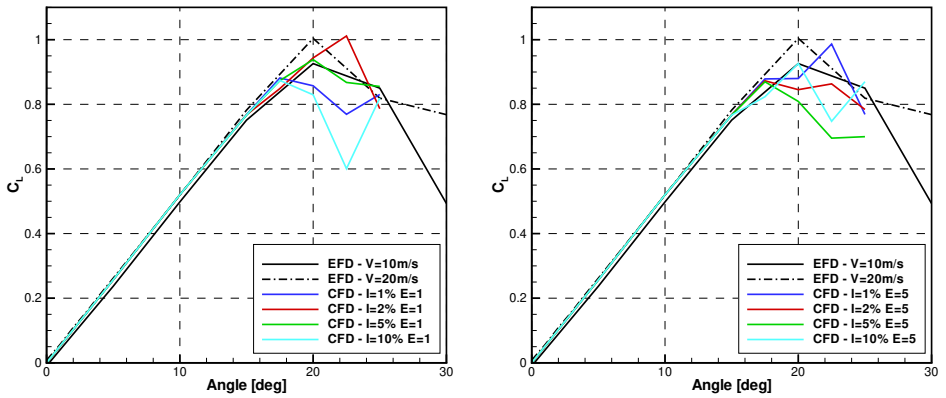

(**a**) Fixed Eddy Viscosity Ratio (E=1) (**b**) Fixed Eddy Viscosity Ratio (E=5)

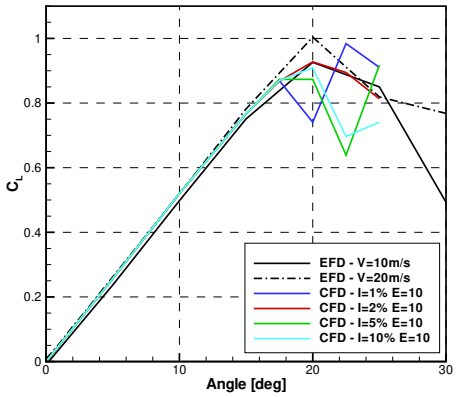

(**c**) Fixed Eddy Viscosity Ratio (E=10)

Figure 10. Numerical influence of the turbulent parameters on the non-dimensional lift.

6. Rudder behind Propeller

Starting from the previously mentioned analyses concerning the adopted propeller model and the rudder numerical set-up, some additional simulations varying the interaction parameters (the propeller load and the rudder/propeller positions) have been carried out and compared with the available experimental measurements ([16,36]).

6.1. Propeller Load Effect

Figure 11 shows, for three considered loads, the comparison between the EFD measurements and the CFD predictions. The measurements were performed at three revolution rates, 800, 1460 and 2100 RPM, with a common value of the velocity in the tunnel, thus varying propeller load, with values of $K_T/J^2 = 0.05, 0.88, 2.3$. Knowing the adopted propeller load, a fixed thrust and torque can be obtained from the propeller open-water curves together with their radial force distributions (as shown in the previous section). Analysing the results collected in Figure 11, a good agreement between the CFD data and the EFD measurements for a wide range of angles is present. As previously, the stall inceptions do not correspond to the experimental ones, even if the tendency is well captured, with stall postponed in correspondence to higher propeller loadings. This further confirms the inability of the proposed method to correctly account this particular aspect. On the contrary, the increase of the lift force due to the propeller interaction is accurately reproduced for all the loads. Some minor discrepancies can be highlighted for the negative range of angles of attack, mainly due to the swirl effect induced by the propeller. In fact, due to the propeller revolutions, some tangential flow components are generated in the propeller slipstream which make the rudder force behaviour not completely

symmetrical with respect to the angle of attack. This effect seems sightly more evident for the EFD measurements instead of the CFD data. In order to have a complete analysis, another aspect has to be considered. The adopted thrust, and consequently the torque, for each simulation has been assumed considering the propeller open-water diagram. Therefore, no interactions of the rudder on the propeller forces has been considered. From the experimental data, at the prescribed revolution rate, also the propeller forces were measured for each rudder angle, thus allowing to have an insight into the possible interactions.

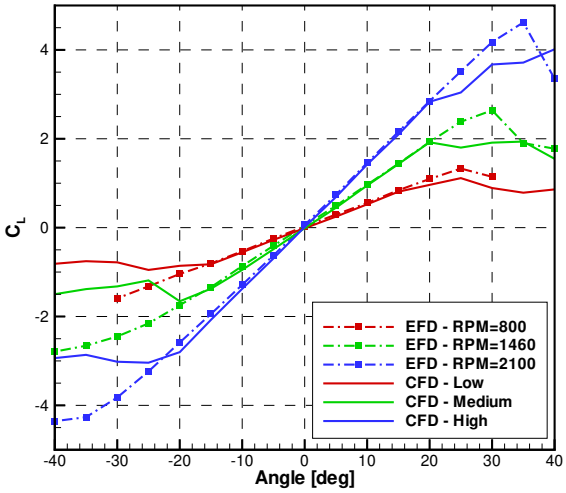

Figure 11. EFD and CFD comparison of rudder lift behind propeller at three loads: equivalent to 800, 1460 and 2100 RPM.

Table 3 summarises the theoretical (the ones computed by the open-water diagram) and the effective (the mean one measured) thrust and torque provided by the propeller. It is evident that the rudder interacts with the propeller force modifying the expected behaviour in open water. In particular, a higher thrust is always experienced by the propeller. It is interesting, on the contrary, that the proposed model correctly predicts the rudder force behaviour imposing the theoretical thrust not the effective one. This could be due to the fact that the two devices interact by means of a pressure field and not velocities, i.e., the rudder overpressure generates an additional propeller force without significantly modifying its inflow velocity field. Further numerical and experimental analysis in this direction are needed to confirm this conclusion. Anyway, this consideration could be important, because, if the rudder forces are of interest, the numerical model can neglect this additional effect. Differently, in the manoeuvring perspective, this aspect assumes quite a low impact.

Table 3. Rudder effect on the propeller forces.

	n (rpm)	K_T/J^2 (-)	T (N)	Q (Nm)
Theoretical	800	0.05	3.92	0.85
	1460	0.88	68.99	8.32
	2100	2.30	180.32	20.23
Measured	800	0.05	7.30	1.25
	1460	0.88	72.12	8.50
	2100	2.30	221.67	23.91

6.2. Propeller Position Effect

Additionally, the relative position between the rudder and the propeller has been investigated (Figure 12). Considering the small variations included in the experimental activities (which amplitude can be extracted from the legends of Figure 12), a wider range of the parameters has been numerically considered. Three parameters were considered: the longitudinal, lateral and vertical propeller position. The first, expressed as X/D, represents the distance of the propeller plane from the leading edge of the rudder at zero-angle. This parameter, from a theoretical point of view (following the actuator disk theory), changes the accelerated flow which is experienced by the rudder. Farther from the propeller plane, the flow tube becomes faster and narrower, as seen in the previous section. The second one is the lateral position, defined by the distance of the propeller axis from the rudder plane at zero-angle (Y/D). This parameter influences the rudder force due to the different portion of the accelerated tube flow which hits the rudder. Increasing the lateral shift reduces the portion of the accelerated flow that affects the rudder. Moreover, due to the propeller tangential components, this effect is asymmetrical with respect to both the rudder angle of attack and to the direction of the lateral shift. Finally, the vertical position, defined as the distance of the propeller axis from the rudder root plane (Z/D), generates a similar effect as the lateral shift. Together with the CFD predictions, also the EFD results have been reported as reference.

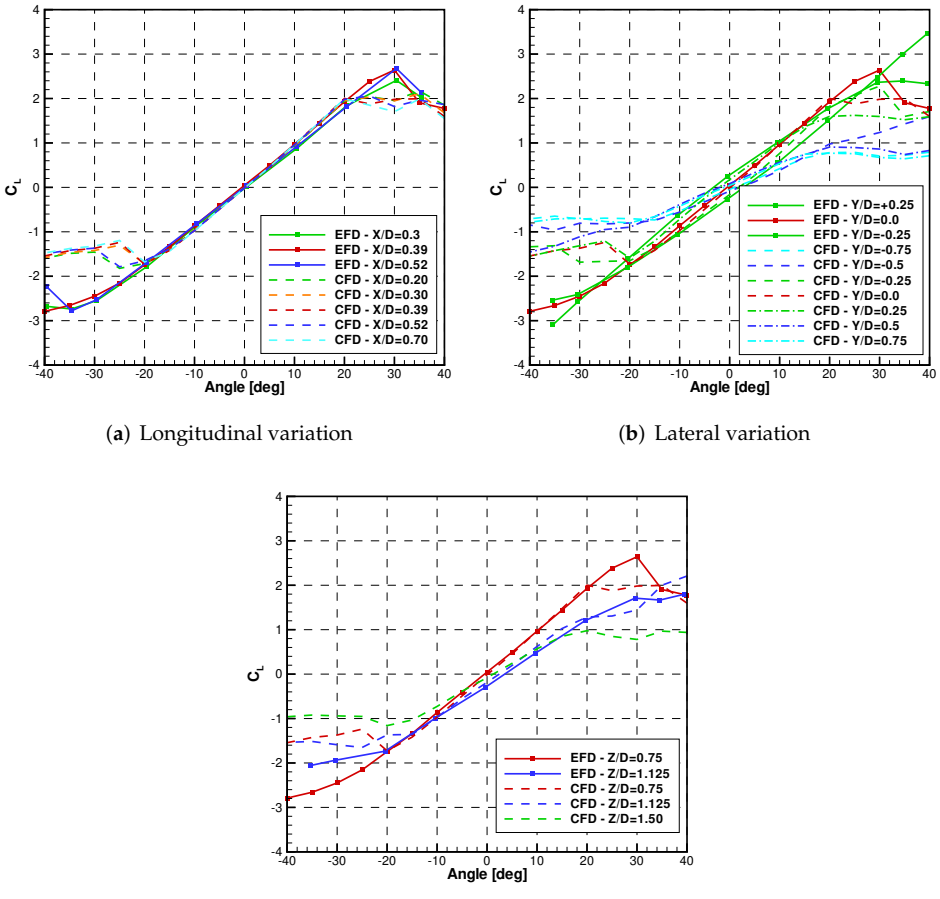

(**a**) Longitudinal variation

(**b**) Lateral variation

(**c**) Vertical variation

Figure 12. EFD–CFD results varying the relative positions between the rudder and the propeller.

Figure 12a shows the effect of the longitudinal position. Both the CFD and EFD results show that the distance between the rudder and the propeller has a negligible effect on the linear part of the data. Some minor effects can be seen only in the stall inception. This is a very interesting aspect. Even though, due to the propeller wake contraction in the range between 0.2 and $0.7X/D$, the tube

area decreases by about 10%, with a corresponding increase of speed, the rudder forces do not change. In the reference literature, this is ascribed to a cancellation effect between the wake contraction and the increased propeller thrust. In the CFD results, considering that a constant thrust is imposed, some effects should be visible. Therefore, in the light of the CFD results obtained, at least for the present cases, another flow mechanism should underlay this insensitivity to the longitudinal distance. For instance because the energy produced by the propeller wake is constant along the tube and proportional to the power delivered by the propeller (or the actuator disc for these simulations). Further analyses are certainly needed to confirm this and the authors plan to continue this study in this direction.

In contrast, Figure 12b shows a strong effect of the lateral position with respect to the rudder provided forces. The CFD behaviour is confirmed by the experimental measurements. Two different effects can be seen. First, the rudder force decreases with increasing lateral shift. This effect is strongly non linear, mainly due to the portion of the rudder hit by the propeller slipstream.

Figure 13 highlights this aspect, showing how the portion of the rudder involved by the accelerated flow of the propeller changes with the lateral shift. These pictures clearly highlight that the expected propeller effect is maximum for the smallest lateral shift ($Y/D = 0; \pm 0.2$) and it strongly decreases (up to zero) for the larger shifts ($Y/D = \pm 0.4; \pm 0.6$). Similar considerations can be seen in the rudder force behaviour: for small shifts, the force does not significantly change, differently, for larger shifts, the rudder works almost as in open-water condition. The second aspect shown by these data concerns the loss of symmetry of the forces. In both the measurements and calculations the rudder lift, at zero angle of attack, assumes values different from zero and proportional to the shift values. This is due to the swirl effect induced by the propeller. The magnitude of this effect is again well captured by the CFD prediction with respect to the literature EFD measurements. Figure 12c again confirms the accuracy of the proposed model. Here, it is well visible as the combined effects, reduction of the rudder portion affected by the accelerated flow and the propeller swirl effect, are well captured by the CFD simulations. It is also interesting to note as the effect of the vertical position is again strongly non linear, despite of the linearity of the interaction area (see Figure 14).

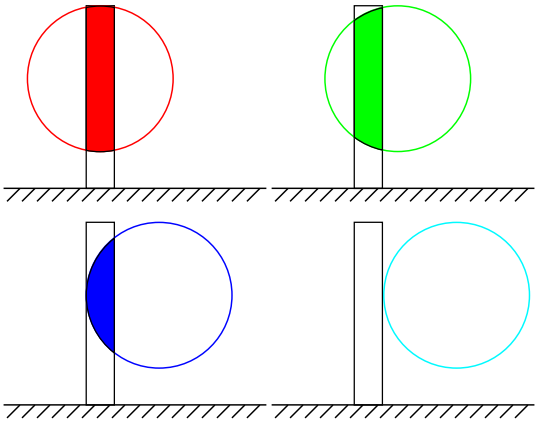

Figure 13. Interaction area varying the lateral position between rudder and propeller. From left to right and top to bottom, respectively, $Y/D = 0; 0.2; 0.4; 0.6$.

This can be mainly due to the radial distribution of the velocities in the flow tube induced by the propeller rotation. In fact, shifting upward the centre of the disk by only about one third of the diameter, its effect on the rudder forces is strongly reduced.

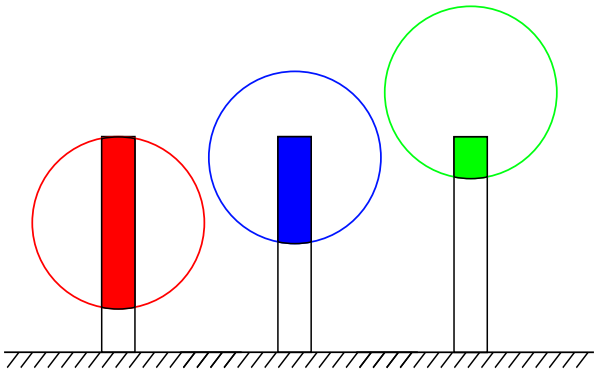

Figure 14. Interaction area varying the vertical position between rudder and propeller. From right to left and top to bottom, respectively, $Z/D = 0.75; 1.125; 1.50$.

7. Rudder–Propeller Model

In the previous section, the ability of the proposed CFD procedure to accurately predict (at least in the pre-stall region) the rudder force, also when it interacts with a propeller, has been demonstrated. In the manoeuvring research field, this aspect is fundamental to correctly predict the manoeuvring ability of a ship, because the rudder is the main device that controls the ship route.

The reference literature adopts a quite crude, but effective, approach. Starting from the knowledge of the rudder performance in free-flow condition, it evaluates the rudder interaction with the propeller by means of the actuator disk theory. First, the propeller accelerated flow to the rudder is evaluated using Equation (5); then, considering that only a portion of the rudder will be affected by the propeller slipstream, the mean flow field to the rudder (U_{Rad}) can be obtained by averaging the two speeds (the accelerated one U_R and the undisturbed one U_S) proportionally to the interested rudder areas (Equation (8)). A sketch of the considered areas can be seen in Figure 15.

$$U_{Rad} = \sqrt{U_R^2 \left(\frac{A_P}{A_R}\right) + U_S^2 \left(1 - \frac{A_P}{A_R}\right)} \tag{8}$$

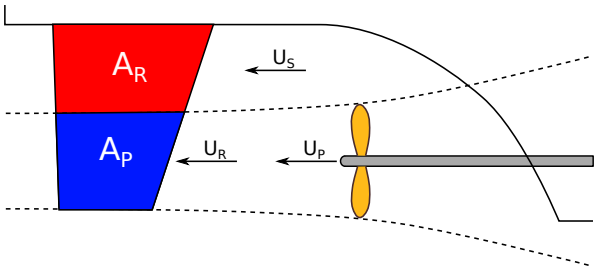

Figure 15. Rudder model quantities.

As extensively reported in literature (see for instance [45] or [46]), the flow acceleration at the rudder section needs to be strongly reduced to some extent (about 40% considering the present experiments), obtaining a new rudder speed given by the Equation (9).

$$U_R^* = k(U_R - U_S) + U_S \tag{9}$$

The meaning of this experimentally tuned coefficient is not completely clear. In addition, its value is strongly connected with the relative size between the rudder and the propeller and slightly also with the distance between the rudder and the propeller. Figure 16 shows the numerical non-dimensional lift force of the rudder at a prescribed angle of attack (15 degrees), varying the propeller size and its load separately. The red lines show the force behaviour applying the original semi-empirical model,

keeping the k coefficient fixed. It is easily seen that its values do not follow the numerically predicted forces, with errors up to 13%.

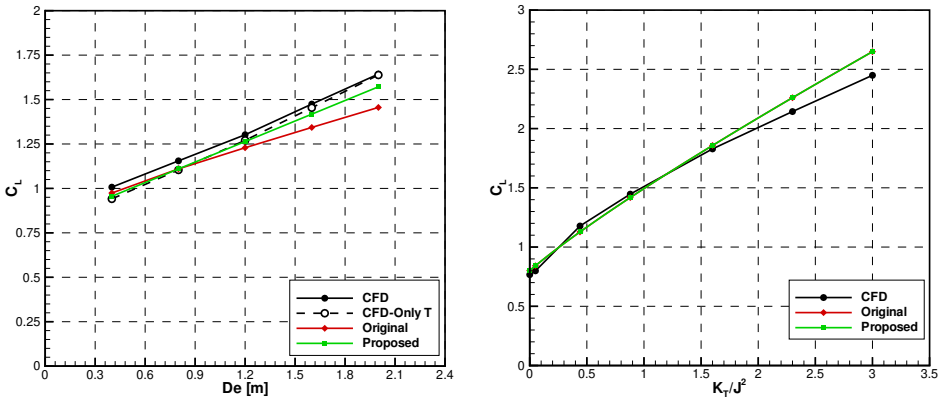

(**a**) with fixed propeller load (**b**) with fixed propeller diameter

Figure 16. Comparison of the original and proposed rudder–propeller models for a single pre-stall angle (15 degrees) versus the CFD results (solid line: complete propeller model; dashed line: only thrust, no torque).

Therefore, a new method has been proposed to increase the trustworthiness of this general approach. Instead of correcting the accelerated flow generated by the propeller at the rudder section, the increased velocity at the propeller section is used. Consequently, the mean flow speed at the rudder can be obtained by the new expression (10):

$$U_{Rad} = \sqrt{U_P^2 \left(\frac{A_P}{A_R}\right) + U_S^2 \left(1 - \frac{A_P}{A_R}\right)} \tag{10}$$

where U_P is the average speed at the propeller plane. In contrast to the original model, also the rudder area affected by the accelerated flow depends only on the propeller diameter. The effectiveness of this new approach is easily seen in Figure 16 (green lines). When a different propeller size is considered, with the same rudder, the new method shows a better agreement with the CFD predictions (the agreement is further increased compared with a pure actuator disk, no torque: dashed line). At the same time (as reported in the lower part of the figure), this proposed approach provides the same results of the original model with respect to a change in propeller load (the two lines are overlapped), without including any experimental corrections. Furthermore, the longitudinal propeller-rudder distance results mathematically irrelevant, as demonstrated by the numerical and experimental data previously reported. For the sake of completeness, the original model is only slightly affected by this longitudinal distance. Figure 17 enlarges the comparison showing how the new model works for all the rudder angles calculated using the three analysed loads.

In conclusion, apparently, at least in the considered cases, the proposed model may be adopted without the need of experiments (or CFD data), fitting better experimental results. It has to be pointed out that this is only a first result, which needs further tests. Therefore, to increase the trustworthiness on this new model, a broader numerical and experimental campaign should be conducted for different rudder shapes and propeller arrangements.

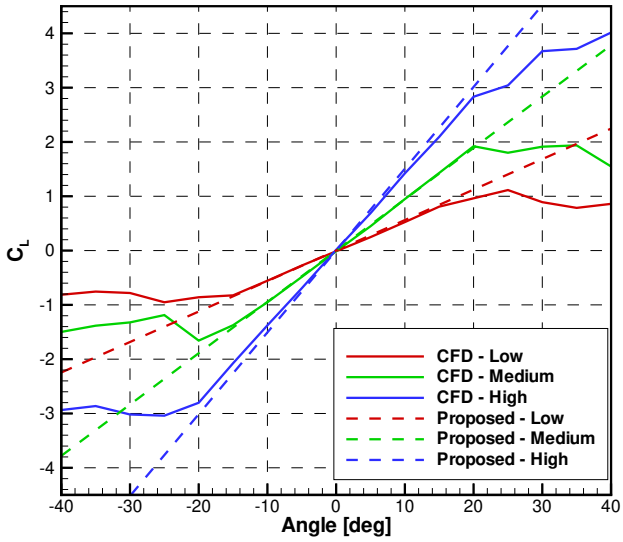

Figure 17. Comparison of the proposed (dashed lines) models versus the computed rudder forces (solid lines).

8. Rudder Sectional Force Analysis

To further enlarge the understanding of the rudder–propeller interaction, additional analyses have been considered focusing the attention on the rudder force distribution. Thanks to the significant amount of data within a CFD simulation, also the rudder force distribution in span-wise direction can be extracted and analysed.

A new rudder shape and test conditions are used to gain a better insight into the problem (Figure 18 shows a sketch). A doubled span characterises the adopted rudder compared to the original one with the same chord length. In addition, the sidewall has been eliminated. These simplifications generate to obtain a rudder which experiences a similar force of the original one (almost the same effective aspect ratio) but with more available space to interact with different propeller sizes. In light of this, a simpler actuator disk with a constant load radial distribution has been considered, positioned in the middle of the rudder span. These simplifications further reduce the extremities effects, to better show how the load changes with respect to the rudder/propeller interaction. With this set-up, five propeller diameters have been explored ranging from 0.4 m up to 2 m (equivalent to 0.2–1.0 in terms of diameter/span ratio). Each propeller provides the same total load, so both the thrust and the torque have been varied accordingly.

Figure 19 shows the non-dimensional force distributions for three angles: 15, 0 and −15 degrees along the rudder span. They were obtained by integrating the stress fields (pressures and wall shear stresses) on different rudder sections, thus obtaining the sectional contribution to the total lift. These selected angles, within the linear region, are able to show how the rudder force distributions change due to the non-symmetrical effect of the flow induced by the torque. As a reference, with a black line, also the rudder load without propeller effect has been included. When the rudder angle is zero, even if the rudder does not provide any lift force, its load is characterised by a significant effect induced by the tangential components generated by the propeller. The same effect is well visible also for the other two analysed conditions, which makes the force distribution strongly non-symmetrical. In the same way, Figure 20 shows the rudder force distribution in the previous condition (limited for only 15 degrees) but neglecting the torque component in the actuator disks (continuous line). Comparing the two figures, it is evident that the two effects (loads induced by to the thrust and the torque) can be linearly superimposed. To further support this conclusion, in Figure 20, with the dashed lines, the previous force distributions subtracting those zero degrees (which are only affected by the tangential components) are reported. Except for a small effect near the propeller hub (most evident for the smallest diameter), the two distributions are in good agreement. These considerations demonstrate

why the mathematical model, though completely neglecting the torque effect, maintains a good agreement with the measurements. Consequently, it is evident by the proposed results that the torque has a small effect on the lift generation (at least in the pre-stall functioning region). On the other hand, it becomes important if other aspects are of interest, for instance cavitation effects or other local effects.

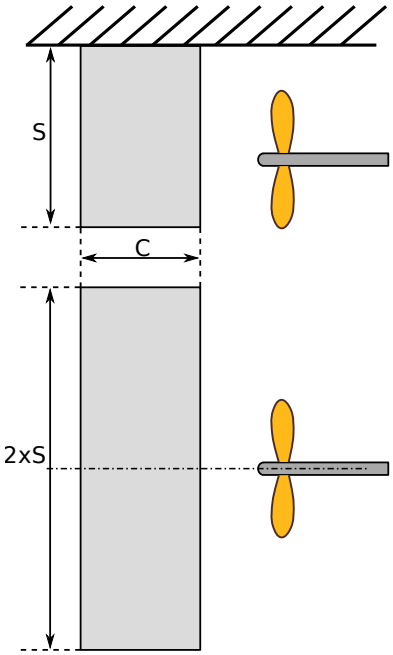

Figure 18. Sketch of the two rudder arrangements.

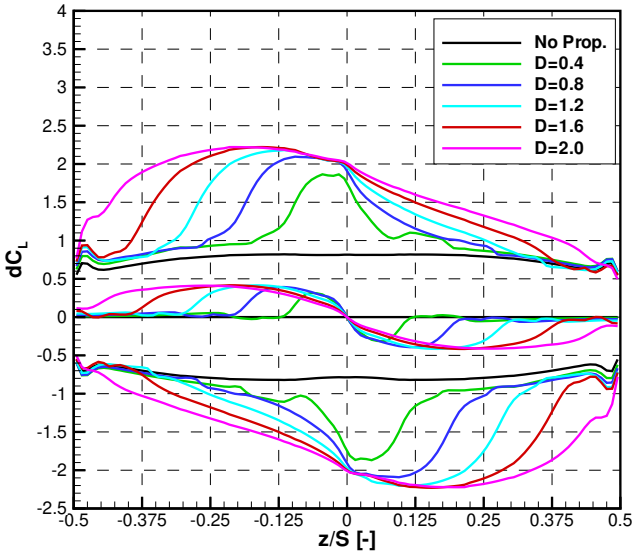

Figure 19. Rudder span-wise force distribution with complete propeller model at three angles of attack: ±15 and 0 degrees.

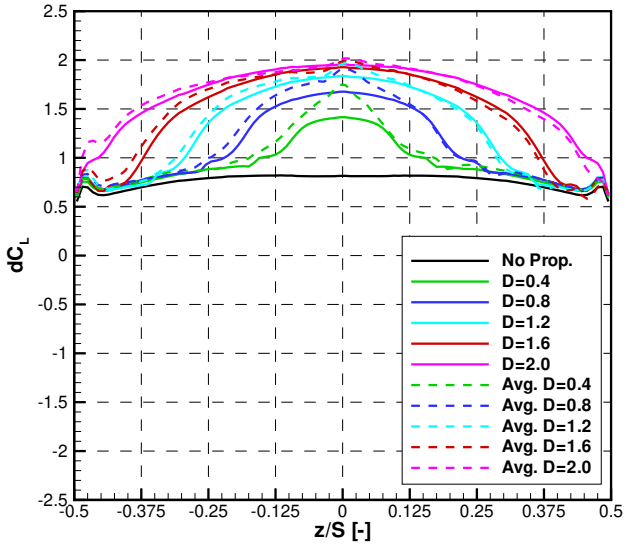

Figure 20. Comparison of the rudder span-wise force distributions without torque (solid lines) and the average force distributions with the complete model (dashed lines) at 15 degrees of rudder angle.

9. Conclusions

This work shows the application of an open-source CFD numerical procedure to predict the interaction between a propeller and a rudder positioned in its slip-stream, considering typical operative conditions during the ship life. Different aspects have been considered to define properly the code ability to tackle this particular problem.

Preliminarily, the flow field generated by the viscous solver, which adopts the body force approach to include the propeller effect in an efficient way, has been compared with classical actuator disk theory, showing its ability to provide more information with respect to this simplified approach. The tube contraction and the expected velocities distribution well match with the theoretical ones.

Then an extensive analysis of the influence of the mesh set-up (in term of wall boundary layer description and turbulent inlet quantities) on the expected numerical results for a wide range of angle of attacks has been considered. These simulations demonstrate that the wall-resolved model better predicts the stall inception but with a quite significant sensitivity on the turbulent parameters. Differently, if the pre-stall region is of interest, both the approaches (wall-resolved and wall-modelled) give the same accuracy with the only constraints to avoid too high turbulent values of the inflow field. Comparing the results with the available measurements, optimal values of turbulent intensity and Eddy Viscosity have been selected obtaining a better CFD/EFD agreement.

Selecting the proper simulations set-up parameters, a systematic analysis of the interactions between the rudder and the propeller varying the propeller load and their mutual position have been carried out comparing the results with respect to the measurements. A very good agreement was found showing that most of the interaction effects are well captured by the CFD predictions. Two are the main additional considerations drawn by the data. First, varying the longitudinal distance between the two devices, the rudder force increment due to the propeller is constant, in contrast with the classical actuator disk theory. Second, the propeller forces seem to vary due to an additional pressure field generated by the rudder, not for a different working condition of the propeller itself. Therefore, if only the rudder forces are of interests, this additional interaction can be neglected without losing accuracy.

Thanks to all these data, a new simplified mathematical model has been developed based on the one typically adopted in the manoeuvring field. Compared to the original one, it does not depends on the longitudinal distance by the propeller and the rudder (as demonstrated by the numerical and experimental measurements) and it works also for different propeller sizes without requiring any calibration parameters.

Finally, analysing the rudder sectional forces when it operates behind propellers with different diameters, the load generated by the accelerated flow (due to the propeller thrust) can be linearly superimposed to the load generated by the tangential flow components (due to the propeller torque). Therefore, if the rudder performances are of interest, the propeller torque can be neglected; differently, if local flow quantities are important, as for cavitation, it has to be included in the analyses.

Author Contributions: Conceptualization, D.V., A.F. and M.V.; methodology, D.V. and A.F.; software, D.V.; validation, D.V.; formal analysis, D.V. and M.V.; investigation, D.V., A.F.; resources, D.V. and M.V; data curation, D.V.; writing–original draft preparation, D.V.; writing–review and editing, M.V.; visualization, D.V.; supervision, M.V. All authors have read and agreed to the published version of the manuscript.

Funding: This research received no external funding.

Conflicts of Interest: The authors declare no conflict of interest.

Abbreviations

The following abbreviations are used in this manuscript:

CFD	Computational Fluid Dynamics
EFD	Experimental Fluid Dynamics
RANS	Reynolds Average Navier–Stokes

References

1. Martelli, M.; Figari, M. Real-Time model-based design for CODLAG propulsion control strategies. *Ocean Eng.* **2017**, *141*, 265–276. [CrossRef]
2. Alessandri, A.; Donnarumma, S.; Luria, G.; Martelli, M.; Vignolo, S.; Chiti, R.; Sebastiani, L. Dynamic positioning system of a vessel with conventional propulsion configuration: Modeling and simulation. In *Maritime Technology and Engineering, Proceedings of the MARTECH 2014: 2nd International Conference on Maritime Technology and Engineering, Lisbon, Portugal, 15–17 October 2014*; Taylor & Francis Group: London, UK, 2015; pp. 725–734. [CrossRef]
3. International Maritime Organization. *Explanatory Notes to the Standards for Ship Manoeuvrability*; MSC/Circ.1053 Adopted 16 December 2002; International Maritime Organization: London, UK, 2002.
4. International Maritime Organization. *Standards for Ship Manoeuvrability*; Resolution MSC. 137 (76); International Maritime Organization: London, UK, 2002.
5. Villa, D.; Viviani, M.; Tani, G.; Gaggero, S.; Bruzzone, D.; Podenzana, C. Numerical Evaluation of Rudder Performance Behind a Propeller in Bollard Pull Condition. *J. Mar. Sci. Appl.* **2018**, *17*, 153–164. [CrossRef]
6. Martelli, M.; Villa, D.; Viviani, M.; Donnarumma, S.; Figari, M. The use of computational fluid dynamic technique in ship control design. *Ships Offshore Struct.* **2019**. [CrossRef]
7. Muscari, R.; Dubbioso, G.; Viviani, M.; Di Mascio, A. Analysis of the asymmetric behavior of propeller–rudder system of twin screw ships by CFD. *Ocean Eng.* **2017**, *143*, 269–281. [CrossRef]
8. Piaggio, B.; Martelli, M.; Viviani, M.; Figari, M. Manoeuvring model and simulation of the non-linear dynamic interaction between tethered ship and tug during escort. In Proceedings of the Maritime Transportation and Harvesting of Sea Resources, Lisbon, Portugal, 9–11 October 2017; Volume 1, pp. 95–104.
9. Figari, M.; Martinelli, L.; Piaggio, B.; Enoizi, L.; Viviani, M.; Villa, D. An all-round design-to-simulation approach of a new Z-drive escort tug class. *J. Offshore Mech. Arct. Eng.* **2020**, *142*, 031107. [CrossRef]
10. Piaggio, B.; Viviani, M.; Martelli, M.; Figari, M. Z-Drive Escort Tug manoeuvrability model and simulation. *Ocean Eng.* **2019**, *191*, 106461. [CrossRef]
11. Villa, D.; Viviani, M.; Gaggero, S.; Vantorre, M.; Eloot, K.; Delefortrie, G. CFD-based analyses for a slow speed manoeuvrability model. *J. Mar. Sci. Technol.* **2019**, *24*, 871–883. [CrossRef]
12. Bruzzone, D.; Ruscelli, D.; Villa, D.; Vivani, M. Numerical prediction of hull force for low velocity manoeuvring. In Proceedings of the 18th International Conference on Ships and Shipping Research (NAV 2015), Lecco, Italy, 24–26 June 2015; pp. 284–295.
13. Suzuki, R.; Tsukada, Y.; Tsujimoto, M.; Muraoka, E.; Ueno, M. A study on high-lift rudder performance in adverse weather based on model tests under high propeller load. *Ocean Eng.* **2017**, *136*, 152–167. [CrossRef]

14. Shin, Y.J.; Kim, M.C.; Lee, J.H.; Song, M.S. A numerical and experimental study on the performance of a twisted rudder with wavy configuration. *Int. J. Nav. Archit. Ocean Eng.* **2019**, *11*, 131–142. [CrossRef]
15. Seo, D.W.; Oh, J.; Jang, J. Performance analysis of a horn-type rudder implementing the Coanda effect. *Int. J. Nav. Archit. Ocean Eng.* **2017**, *9*, 177–184. [CrossRef]
16. Molland, A.; Turnock, S. *Wind Tunnel Investigation of the Influence of Propeller Loading on Ship Rudder Performance*; Project Report; University of Southampton: Southampton, UK, 1991; ISSN 0140-3818.
17. Li, D.Q. A non-linear method for the propeller-rudder interaction with the slipstream deformation taken into account. *Comput. Methods Appl. Mech. Eng.* **1996**, *130*, 115–132. [CrossRef]
18. He, L.; Kinnas, S.A. Numerical simulation of unsteady propeller/rudder interaction. *Int. J. Nav. Archit. Ocean Eng.* **2017**, *9*, 677–692. [CrossRef]
19. Li, D.Q. *Investigation on Propeller-Rudder Interaction by Numerical Methods*; Chalmers University of Technology: Göteborg, Sweden, 1994.
20. Nakatake, K.; Koga, T.; Yamazaki, R. On the Interaction between Screw Propeller. In *Transactions of the West-Japan Society of Naval Architects*; The Japan Society of Naval Architects and Ocean Engineers: Tokyo, Japan, 1981.
21. Turnock, S. Prediction of ship rudder-propeller interaction using a panel method. In Proceedings of the 19th WEGEMT School on Numerical Simulation of Hydrodynamics: Ships and Offshore Structures, Propeller and Lifting Surfaces, Nantes, France, 20–24 June 1993.
22. Badoe, C.E.; Phillips, A.B.; Turnock, S.R. Influence of drift angle on the computation of hull–propeller–rudder interaction. *Ocean Eng.* **2015**, *103*, 64–77. [CrossRef]
23. Liu, J.; Quadvlieg, F.; Hekkenberg, R. Impacts of the rudder profile on manoeuvring performance of ships. *Ocean Eng.* **2016**, *124*, 226–240. [CrossRef]
24. Guo, H.P.; Zou, Z.J.; Liu, Y.; Wang, F. Investigation on hull-propeller-rudder interaction by RANS simulation of captive model tests for a twin-screw ship. *Ocean Eng.* **2018**, *162*, 259–273. [CrossRef]
25. Phillips, A.B.; Turnock, S.R.; Furlong, M. Accurate Capture of Propeller-Rudder Interaction using a Coupled Blade Element Momentum-RANS Approach. *Ship Technol. Res.* **2010**, *57*, 128–139. [CrossRef]
26. Calcagni, D.; Bellotto, F.; Broglia, R.; Salvatore, F.; Bensow, R. Comparative analysis of the hydrodynamic performance of untwisted and twisted rudders using a hybrid RANSE/BEM model. In Proceedings of the International Offshore and Polar Engineering Conference, Busan, Korea, 15–20 June 2014.
27. Van Nguyen, T.; Ikeda, Y. Development of fishtail rudder sections with higher maximum lift coefficients. In Proceedings of the Twenty-Fourth International Ocean and Polar Engineering Conference, Busan, Korea, 15–20 June 2014.
28. Liu, J.; Quadvlieg, F.; Hekkenberg, R. Impacts of rudder profiles on ship manoeuvrability. In Proceedings of the International Conference on Marine Simulation and Ship Maneuverability, Newcastle upon Tyne, UK, 8–11 September 2015.
29. Ferrando, M.; Gaggero, S.; Villa, D. Open source computations of planing hull resistance. *Trans. R. Inst. Nav. Archit. Part Int. J. Small Craft Technol.* **2015**, *157*, 83–98. [CrossRef]
30. Piaggio, B.; Villa, D.; Viviani, M. Numerical analysis of escort tug manoeuvrability characteristics. *Appl. Ocean. Res.* **2020**, *97*. [CrossRef]
31. Piaggio, B.; Villa, D.; Viviani, M.; Figari, M. Numerical analysis of escort tug manoeuvrability characteristics—Part II: The skeg effect. *Appl. Ocean. Res.* **2020**, *100*, 102199. [CrossRef]
32. Villa, D.; Gaggero, S.; Gaggero, T.; Tani, G.; Vernengo, G.; Viviani, M. An efficient and robust approach to predict ship self-propulsion coefficients. *Appl. Ocean. Res.* **2019**, *92*, 101862. [CrossRef]
33. Peskin, C.S. Flow patterns around heart valves: A numerical method. *J. Comput. Phys.* **1972**, *10*, 252–271. [CrossRef]
34. Hu, J.; Zhang, W.; Sun, S.; Guo, C. Numerical simulation of Vortex–Rudder interactions behind the propeller. *Ocean Eng.* **2019**, *190*, 106446. [CrossRef]
35. Gaggero, S.; Gaggero, T.; Tani, G.; Vernengo, G.; Viviani, M.; Villa, D. Ship self-propulsion performance prediction by using OpenFOAM and different simplified propeller models. In *Progress in Maritime Technology and Engineering, Proceedings of the 4th International Conference on Maritime Technology and Engineering, (MARTECH), Lisbon, Portugal, 7–9 May 2018*; Taylor & Francis Group: London, UK, 2018; pp. 195–206. [CrossRef]

36. Molland, A.; Turnock, S. *Further Wind Tunnel Tests on the Influence of Propeller Loading On Ship Rudder Performance*; Project Report; University of Southampton: Southampton, UK, 1992; ISSN 0140-3818.
37. Molland, A.; Turnock, S. *Wind Tunnel Test Results for a Model Ship Propeller Based on A Modified Wageningen b4.40*; Project Report; University of Southampton: Southampton, UK, 1990; ISSN 0140-3818.
38. Gaggero, S.; Villa, D. Cavitating Propeller Performance in Inclined Shaft Conditions with OpenFOAM: PPTC 2015 Test Case. *J. Mar. Sci. Appl.* **2018**, *17*, 1–20. [CrossRef]
39. Villa, D.; Gaggero, S.; Tani, G.; Viviani, M. Numerical and experimental comparison of ducted and non-ducted propellers. *J. Mar. Sci. Eng.* **2020**, *8*, 257. [CrossRef]
40. Brix, J. *Manoeuvring Technical Manual*; Schiff und Hafen; The National Academies of Sciences, Engineering, and Medicine: Washington, DC, USA, 1987; ISSN 0036-603X.
41. Wei, M.; Chiew, Y.M. Impingement of propeller jet on a vertical quay wall. *Ocean Eng.* **2019**, *183*, 73–86. [CrossRef]
42. Felli, M.; Falchi, M.; Fornari, P.; Pereira, F.J.A. PIV Measurements on an Impinging Swirl Jet in a Large Cavitation Tunnel. In Proceedings of the 14th International Symposium on Applications of Laser and Imaging Techniques to Fluid Mechanics (LISBON'08), Lisbon, Portugal, 7–10 July 2008.
43. Glauert, H. *The Elements of Aerofoil and Airscrew Theory*; Cambridge Science Classics, Cambridge University Press: Cambridge, UK, 1983. [CrossRef]
44. Ahn, T.; Kim, C.; Rho, O.H. Dynamic-stall control based on an optimal approach. *J. Aircr.* **2004**, *41*, 1106–1116. [CrossRef]
45. Yasukawa, H.; Yoshimura, Y. Introduction of MMG standard method for ship maneuvering predictions. *J. Mar. Sci. Technol.* **2014**, *20*, 37–52. [CrossRef]
46. Martelli, M. *Marine Propulsion Simulation*; Walter de Gruyter GmbH: Berlin, Germany, 2015; pp. 1–104.